Biosensors and Bioelectronics 134 (2019) 1–7

Contents lists available at ScienceDirect

Biosensors and Bioelectronics

journal homepage: www.elsevier.com/locate/bios

All-solid-state metal-mediated Z-scheme photoelectrochemical immunoassay with enhanced photoexcited charge-separation for monitoring of prostate-specific antigen

Lijia Zhang[a], Zhongbin Luo[a], Ruijin Zeng[a], Qian Zhou[b,*], Dianping Tang[a,**]

[a] Key Laboratory for Analytical Science of Food Safety and Biology (MOE & Fujian Province), State Key Laboratory of Photocatalysis on Energy and Environment, Department of Chemistry, Fuzhou University, Fuzhou, 350116, PR China

[b] Institute of Environmental and Analytical Science, School of Chemistry and Chemical Engineering, Henan University, Kaifeng, 475004, Henan, PR China

ARTICLE INFO

Keywords:
Photoelectrochemical immunoassay
Z-Scheme photosensitive material
WO_3-Au-CdS
Solid electron mediator
Effective charge-separation

ABSTRACT

An all-solid-state metal-mediated Z-scheme photoelectrochemical (PEC) immunoassay was designed for sensitive detection of prostate-specific antigen (PSA) by using WO_3-Au-CdS nanocomposite as photoactive material and copper ion (Cu^{2+}) as an inhibitor. The Z-scheme PEC system comprising of CdS nanoparticle (photosystem I; PS I), WO_3 nanorod (photosystem II; PS II) and gold nanoparticle (Au NP; solid electron mediator) was reasonably established by a simple and green synthetic method. As an important part of Z-scheme system, the sandwiched gold nanoparticles between electron donor materials and hole provider materials could accelerate electron transfer from positive conduction band (CB) of WO_3 to negative valence band (VB) of CdS, thus resulting in high-efficient separation of the carriers. In the presence of target PSA, a sandwiched immunoreaction was executed between capture antibody-coated microplate and CuO nanoparticle-labeled detection antibody. Thereafter, CuO nano labels were dissolved into Cu^{2+} ions under acidic condition to decrease the photocurrent of Z-scheme WO_3-Au-CdS thanks to the formation of exciton trapping center of Cu_xS (x = 1,2) on the surface. Under optimum conditions, Z-scheme PEC immunoassay exhibited good photocurrents toward target PSA within a linear range of 0.01–50 ng mL^{-1} at a limit of detection of 1.8 pg mL^{-1}. Moreover, the Z-scheme PEC immunoassay had high selectivity and accuracy. Importantly, this method provides a new horizon for detection of disease-related biomarkers with high sensitivity.

1. Introduction

With the growing demands on detection of the trace analytes, developing an advanced and highly selective method with future social development is particularly significant. Photoelectrochemical (PEC) sensing system, as a newly emerged yet useful analytical technique, has promptly attracted great attention because to its superior performances, such as higher sensitivity and lower background signal (Kong et al., 2018; Tu et al., 2016; Zhao et al., 2017). In this regard, PEC strategies have been widely utilized in many research fields such as biological analysis and food safety monitoring (Wang et al., 2017a). During the photon-to-electricity signal-conversion process, the electron-hole pairs of the photoactive materials are initially separated, and the electron/hole then transfers to the electrode interface under light irradiation (Qiu et al., 2018; Zhao et al., 2015). The output photocurrent signal, referring to the charge separation, is changed upon the introduction of electron acceptor/donor *via* the biological reaction (Luo et al., 2018; Sun et al., 2014; Zhao et al., 2014). To improve the detectable sensitivity, the low electron-hole recombination is desired (Gao et al., 2018). Despite many advances in this field, there is still the challenge to realize low electron-hole recombination for the development of PEC sensing schemes. To this end, it is the urgent requirement for exploiting ingenious and efficient protocols and strategies to enhance the effective separation of carriers, *e.g.*, by using an artificial Z-scheme photoexcited system mimicking the photosynthesis of the plants.

Naturally, plants can effectively achieve solar-to-chemical energy conversion accompanying two sequential photoexcited charge-separation processes, followed by a Z-scheme principle (Kothe et al., 2013; Wang et al., 2018). The chlorophylls in photosystem II (PS II; as reaction center) firstly capture the light ($\lambda \leq 680$ nm) to generate the electron-hole pairs. The photoinduced holes are used for water splitting to produce O_2, whereas the as-produced electrons are passed to the

* Corresponding author.
** Corresponding author.
E-mail addresses: zhouqian@henu.edu.cn (Q. Zhou), dianping.tang@fzu.edu.cn (D. Tang).

https://doi.org/10.1016/j.bios.2019.03.052
Received 8 March 2019; Accepted 26 March 2019
Available online 29 March 2019
0956-5663/

valence band (VB) of the photosystem I (PS I) through an electron transport chain to produce a chemiosmotic potential for the formation of ATP. Also, the charges are capable of separation in PS I upon light harvesting ($\lambda \leq 700$ nm). Meanwhile, the photoinduced holes in PS I are quenched by the generated electrons from PS II, and the homologous electrons are combined with the nicotinamide adenine dinucleotide phosphate ($NADP^+$) to produce NADPH. The formed NADPH together with ATP is desired to convert CO_2 to sugars (Barber, 2009; Favereau et al., 2016; Yun et al., 2011). One major advantage of using Z-scheme photosynthesis system is that the charge-separation quantum efficiency of this process approaches ~100% (Tachibana et al., 2012). Inspired by the photosynthesis, an artificial Z-scheme photocatalytic system can be designed by coupling two narrow-band gap semiconductors for improving utilization of visible light with an electron mediator (*e.g.*, gold nanoparticles; Au NPs). To effectively operate this system, one critical issue is selecting an appropriate electron mediator to realize efficient electron relay in a Z-scheme system (Iwase et al., 2011; Tada et al., 2006). Compared with common aqueous mediators, the solid electron mediators (*e.g.,* graphene oxide, carbon dots and Au NPs) are capable of avoiding backward reaction and exhibit superiority in stability (Iwase et al., 2016; Li et al., 2016; Zhou et al., 2014). Recently, all-solid-state Z-scheme systems have been widely reported in the fields of water splitting (Wang et al., 2017b), CO_2 conversion (Li et al., 2015) and biosensors (Lv et al., 2018). Liang et al. (2018) prepared Au@g-C_3N_4/SnS yolk-shell Z-scheme photocatalyst for reduction of CO_2 with a Z-scheme system. Wang et al. (2016) combined $SrTiO_3$:La,Rh/$BiVO_4$:Mo with Au NPs for water splitting. Also, our group recently constructed a Z-scheme PEC aptasensing system along with a signal-amplification strategy on the basis of DNA walker (Lv et al., 2018). Unfortunately, this process is time-consuming, and nucleic acid-related signal amplification requires very stringent control for their self-assembled process. Therefore, our motivation of this study is to explore a suitable optoelectronic material and signal-changed mode for construction of Z-scheme PEC platform.

Herein, we report on a double photosystem-excited Z-scheme PEC immunoassay for the sensitive detection of prostate-specific antigen (PSA; as a model analyte in disease-related biomarkers), using WO_3-Au-CdS-based Z-scheme photoactive materials (Scheme 1). In this system, cadmium sulfide (CdS; a favorable narrow band gap of ~2.4 eV) and tungsten oxide (WO_3; a favorable narrow band gap of 2.4–2.8 eV) are served as the PS I and PS II for visible light absorption, respectively. Gold (Au) nanoparticles are employed as efficient solid electron mediators. Under visible-light (the large proportion of total solar energy) irradiation, WO_3 and CdS generate electron-hole pairs, respectively. The sandwiched Au between WO_3 and CdS expedites effective electron relay since the electrons in the conduction band (CB) of WO_3 are easily migrated to Au and captured by the valence band (VB) of CdS. The special electron shuttle efficiently shortens the surviving time of free electrons and holes between the CB of CdS and the VB of WO_3, thus increasing the photocurrent. Additionally, a simple sandwiched immunoreaction in the capture antibody-coated microplate is carried out by using CuO nanoparticle-labeled antibody as the signal tracer. Subsequently, CuO nanoparticles are dissolved under acidic condition to release copper ion, following by rapid reduction reaction of Cu^{2+} ($Cu^{2+} \rightarrow Cu^{+}$) under the illumination (Wang et al., 2010). In this case, Cu_xS ($x = 1,2$; as the exciton trapping sites) generates on Z-scheme photosensitive electrode by a chemical displacement reaction between Cu^{2+}/Cu^{+} and Cd^{2+} (Liu et al., 2015). Because of the electron-hole recombination occurring in the introduced new energy level (Cu_xS), the photocurrent significantly reduces. In this way, a WO_3-Au-CdS-mediated Z-scheme PEC immunosensing platform is established for the quantitative detection of PSA by measuring the change of this system in the photocurrent relative to PSA concentration.

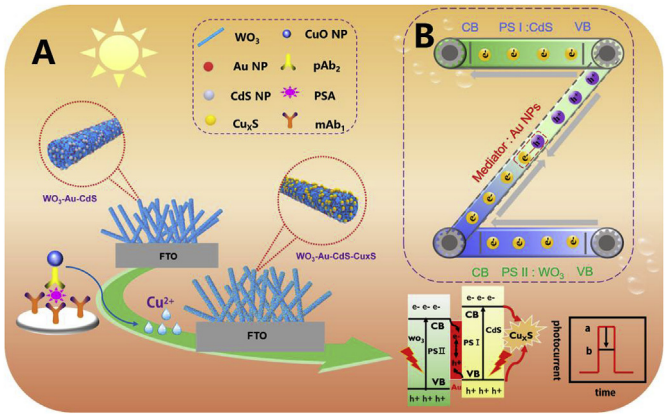

Scheme 1. (A) Schematic illustration of WO_3-Au-CdS-based Z-scheme photoelectrochemical immunosensing platform, and (B) enhanced photoexcited charge-separation process for WO_3-Au-CdS-based Z-scheme system.

2. Experimental

2.1. Chemical and reagent

Monoclonal anti-PSA capture antibody (mAb), polyclonal anti-PSA detection antibody (pAb) and humans PSA ELISA kit including PSA standards with different concentrations were purchased from Biosynth. Biotechnol. Co., Ltd (Beijing, China). $HAuCl_4{\cdot}4H_2O$, $Na_2S{\cdot}9H_2O$ and $Na_2WO_4{\cdot}2H_2O$ were purchased from Sinopharm Chem. Re. Co., Ltd. (Shanghai, China). Bovine serum albumin (BSA), CuO nanoparticles (~50 nm in diameter), $Cd(NO_3)_2{\cdot}6H_2O$ and phosphate-buffered saline (PBS) buffer were the products of Sigma-Aldrich. Na_2CO_3 buffer solution (0.05 M, pH 9.6) was acquired by adding the chemicals (0.2 g NaN_3, 2.93 g $NaHCO_3$ and 1.59 g Na_2CO_3) into ultrapure water (1000 mL). All the high-binding polystyrene 96-well microplates were achieved from Greiner Bio-One (Frickenhausen, 705071, Germany). The washing and blocking buffer solutions were prepared by adding BSA (1.0%, w/v) and Tween 20 (0.05%, v/v) to PBS solution (0.01 M, pH 7.4), respectively. All other reagents were of analytical grade and used without purification. Ultrapure water purified by a Millipore water purification system (18.2 MΩ cm, Milli-Q, Millipore) was used in all runs.

2.2. Synthesis of WO_3 nanorods

WO_3 nanorods (NRs) were prepared through typical hydrothermal treatment according to the report (Jiang et al., 2017). Initially, 0.107 M $Na_2WO_4{\cdot}2H_2O$ and 0.53 M NaCl were dissolved in ultrapure water with continuous stirring, and then HCl aqueous solution was injected to adjust the pH of the mixture for reaching pH 2. Following that, the mixture was stirred for 2 h to form a homogeneous solution. The final reaction was carried out in a 100-mL Teflon-lined autoclave at 180 °C for 24 h. After cooling to room temperature, the obtained product was centrifuged at 10,000 *g* for 10 min and washed with ultrapure water. The as-prepared WO_3 nanorods (precipitates) were dried at 60 °C for use.

2.3. Preparation of WO_3-Au-CdS-modified fluorine-doped tin oxide (FTO) electrode

Prior to preparation, fluorine-doped tin oxide (FTO) electrode was first washed by using ultrapure water, ethanol and acetone in sequence under sonication, and then dried at 50 °C. Following that, 30 μL of WO_3 suspension (4.0 mg mL^{-1}; dispersed in ultrapure water) was dropped on the cleaned FTO electrode (Active area: 0.28 cm^2) and dried at 60 °C. Next, gold nanoparticles deposited onto the resulting electrode by using a simple reduction method in 10 mM pH 4.5 $HAuCl_4$ aqueous solution (note: The pH of $HAuCl_4$ aqueous solution was adjusted to 4.5 by using

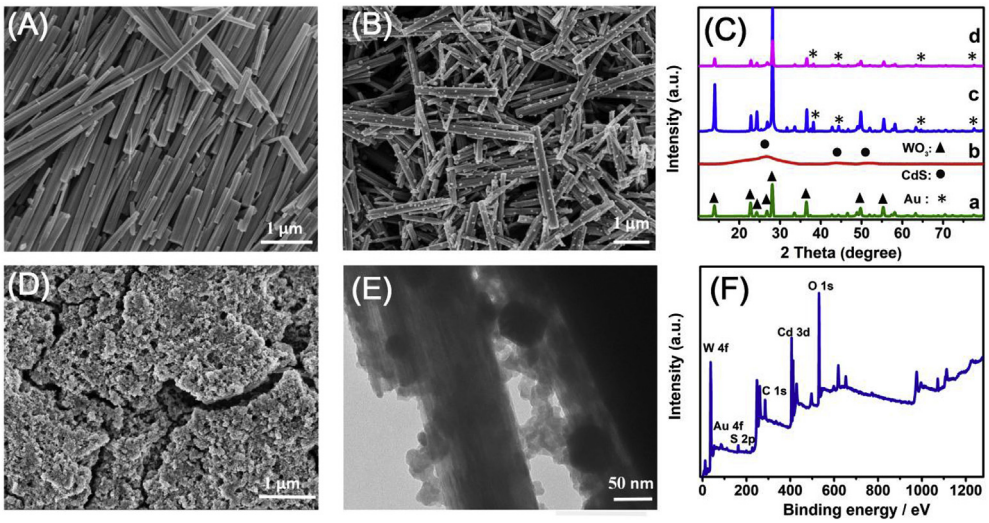

Fig. 1. SEM images of (A) WO_3-, (B) Au-WO_3- and (D) CdS-Au-WO_3-modified FTO electrode; (C) XRD patterns of (a) WO_3, (b) CdS, (c) Au-WO_3 and (d) CdS-Au-WO_3; (E) TEM image and (F) XPS pattern of CdS-Au-WO_3 nanocomposites.

NaOH) (Pu et al., 2013). After washing with ultrapure water, the as-prepared Au-WO_3-modified FTO electrode was used for the deposition of CdS nanoparticles on the surface consulting to the literature (Fan et al., 2014; Tang et al., 2015). Detailedly, the Au-WO_3-modified FTO electrode was initially immersed in a methanol solution containing 0.1 M $Cd(NO_3)_2$, and incubated for 60 s at room temperature. Thereafter, the resultant electrode was transferred to methanol/water (1 : 1, v/v) solution containing 0.1 M Na_2S for another 60 s. The above two-step dipping process was regarded as one-time coating, and the coating process was repeated four times. Finally, CdS-Au-WO_3-modified FTO electrode was washed with methanol and ultrapure water, and stored in a closed 7.0-mL centrifugal tube at 4 °C for further usage.

2.4. Preparation of CuO nanoparticle-labeled pAb detection antibody (CuO NP-pAb)

CuO nanoparticle-labeled pAb detection antibody (CuO NP-pAb) was prepared similar to previous works with minor modification (Qu et al., 2011; Yang et al., 2018). Initially, 1.0 mg of the purchased CuO NP powder was dispersed in PBS (1.0 mL, 10 mM) under sonication (~15 min), and then 200 μL of 0.5 mg mL^{-1} pAb detection antibody was injected into the suspension. Note that the mixture was slightly shaken for 3 h on a shaker at 4 °C. During this process, pAb detection antibody was physically adsorbed to the surface of CuO nanoparticles. Excess antibodies were removed through centrifugation (15 min, 10,000 *g*, 4 °C). Finally, the obtained CuO NP-pAb conjugates were dispersed in PBS (1.0 mL, pH 7.4, 10 mM) containing 1.0 wt % BSA, and stored at 4 °C until use.

2.5. Immunoreaction protocol and PEC measurement

Scheme 1 represents the schematic illustration of the photoelectrochemical immunoassay toward target PSA by coupling CuO-labeled detection antibody with Z-scheme WO_3-Au-CdS photoactive materials. Prior to measurement, mAb-coated microplate was prepared as follows. The mAb capture antibody (50 μL per well, 10 μg mL^{-1}) was initially injected to a high-binding 96-well microtiter plate. Then the resulting microplate was covered with adhesive plastics plate sealing film and incubated overnight at 4 °C. After washing with the washing buffer, mAb-coated microplate was incubated with the blocking buffer (300 μL per well) for 60 min at 37 °C. The resulting microplate was washed as before. Following that, 50 μL of PSA standard/sample was added into the well and incubated for 40 min at 37 °C with slight shaking on a shaker (note: The different-concentration PSA standards or samples were prepared by diluting with 0.1 M PBS, pH 7.4). After washing with the washing buffer, 50 μL of the above-prepared CuO NP-pAb suspension was injected into the well and reacted for 40 min under the same conditions to form the sandwiched immunocomplexes. Following that, 20 μL of 1.0 mM HCl was thrown in the well after washing as before, and reacted for 10 min at room temperature. Subsequently, the resulting mixture containing the as-released copper ion (Cu^{2+}) was transferred to 5.0 mL PBS (0.1 M, pH 7.0) in a transparent beaker for photocurrent measurement. The photoelectrochemical measurement was carried out on a CHI 630D Electrochemical Workstation (CH Instruments Inc., Shanghai, China) equipped with a 500-W Xe lamp (as the light source) at the applied potential of 0 V by using WO_3-Au-CdS-modified FTO electrode as the working electrode, a Pt wire as the auxiliary electrode and a saturated calomel electrode (SCE) as the reference electrode. All the data referred to the average response of reaction with the corresponding standard deviation (Mean ± SD) in triplicate, unless otherwise indicated. All measurements were performed at room temperature (25 ± 1.0 °C).

3. Results and discussion

3.1. Characterization of WO_3-Au-CdS-modified FTO electrode

In this system, the photocurrent was produced on the WO_3-Au-CdS-modified FTO electrode. To investigate the surface morphologies of different components-modified FTO electrodes, we used scanning electron microscopy (SEM; JEOL-3010, Japan) and transmission electron microscope (TEM; Hitachi 7700, Japan) to characterize the as-synthesized WO_3, Au-WO_3 and CdS-Au-WO_3 nanostructures, respectively. As seen from SEM image in Fig. 1A, the as-prepared WO_3 nanomaterials displayed the rod-like structure. Upon reduction of $HAuCl_4$, numerous nanoparticles with a mean size of 30–40 nm in diameter were evenly dispersed on the surface of WO_3-modified FTO electrode (Fig. 1B), preliminarily suggesting the formation of gold nanoparticles. Moreover, another additonal layer of nanostructures was also observed on the Au-WO_3-modified FTO electrode after interaction of the resulting electrode with the mixture containing $Cd(NO_3)_2$ and Na_2S (Fig. 1D). Meanwhile, the thickness and roughness of the modified layer increased to some extent. In addition, the sandwiched CdS-Au-WO_3 nanostructures could clearly observed, as shown from TEM image in Fig. 1E. Many CdS and gold nanoparticles were enwrapped around the WO_3 nanorods with a good interfacial contact. Such a topological structure

can provide a facilitation for the construction of Z-scheme photoactive materials.

Logically, one puzzling question arises as to whether the as-prepared materials derived from the intrinsic WO_3, Au and CdS because it is difficultly confirmed on the results of SEM and TEM. In this case, we utilized X-ray diffraction (XRD) to investigate the crystal structures of the as-obtained products including WO_3, CdS, WO_3-Au and WO_3-Au-CdS (Fig. 1C). Curve '*a*' gives typical XRD pattern of WO_3 nanorods, which well matched with the hexagonal-phase of pure WO_3 (JCPDS card 75–2187) (Weng et al., 2014). The WO_3 NRs with exceedingly strong and sharp diffraction peaks had a well crystallinity. The peaks at 26.6°, 44.0°, and 51.9° (marked with "•") in the XRD pattern of pure CdS NPs (Fig. 1C, curve '*b*') corresponded to the (111), (220), and (311) crystal planes of cubic-phase CdS (JCPDS card 65–2887), respectively (Jiang et al., 2013). In contrast, four peaks at 38.2°, 44.4°, 64.6° and 77.5° (marked with "*") in the XRD patterns of WO_3-Au (curve '*c*') and WO_3-Au-CdS (curve '*d*') samples were correspond to the crystal planes of (111), (200), (220) and (311) of cubic Au (JCPDS card 04–0784) (Park et al., 2013), indicating the formation of gold nanoparticles. However, we did not seemly find the crystal planes of CdS nanostructures in the XRD pattern of WO_3-Au-CdS (curve '*d*' *vs.* Curve '*b*'). The reason might be most likely as a consequence of the fact that the characteristic peaks of CdS nanostructures were partially obscured by the characteristic peaks of WO_3. Significantly, the components of WO_3-Au-CdS could be proved by X-ray photoelectron spectroscopy (XPS) (Fig. 1F), suggesting the existence of W, O, Au, Cd and S elements in the nanostructures. The C element in the XPS spectrum originated from the CO_2 absorbed on the sample. High-resolution XPS spectra of all elements are described in Fig. S1 of the Supporting Information. On the basis of these results, we might make a conclusion that WO_3-Au-CdS nanostructures could be successfully synthesized by using our designed route.

3.2. Photoelectrochemical characterization of CdS-Au-WO_3-modified FTO electrode

As mentioned above, CdS-Au-WO_3-modified FTO electrode played an important role during the PEC measurement. The photocurrent could be generated under light irradiation. Prior to measurement, we used electrochemical impedance spectroscopy (EIS) to investigate the fabrication process of CdS-Au-WO_3-modified FTO electrode after each step (Fig. 2A). Typically, the charge-transfer resistance can be calculated on the basis of the diameter of the semicircle in the Nyquist diagram. Plots '*a*' represents the Nyquist diagram of the cleaned FTO electrode. After coating with WO_3 nanorods on the FTO electrode, the resistance of the resulting electrode (plots '*b*') heavily increased in comparison with that of plots '*a*', indicating that WO_3 nanorods had weak conductivity. After formation of gold nanoparticles on the WO_3-modified FTO electrode, significantly, the resistance of largely decreased (plots '*c*'), suggesting that the deposited gold was favorable for the electron transfer. Furthermore, modification of the subsequent CdS nanoscales caused the increasing resistance of the modified electrode (plots '*d*' *vs.* plots '*c*'). These results revealed that CdS-Au-WO_3 could be immobilized on the FTO electrode.

Another question for the development of Z-scheme PEC sensing strategy is whether the prepared CdS-Au-WO_3 nanocomposites could enhance the electron transfer and charge separation on the FTO electrode by gold and CdS nanoparticles. To clarify this issue, the photocurrent characteristics of the differently modified electrodes were investigated in PBS (0.1 M, pH 7.0) (Fig. 2B). Curve '*a*' shows the photocurrent (~94.3 nA) of WO_3-modified FTO electrode. In contrast, the photocurrent increased to 373 nA after gold nanoparticles were coated onto the WO_3/FTO electrode (curve '*b*'), indicating that gold nanoparticles could facilitate electron transfer and electron-hole pairs. Favorably, the photocurrent largely increased after the formation of Z-scheme CdS-Au-WO_3 on the FTO electrode (curve '*c*'). Moreover, the absence of gold nanoparticles between WO_3 and CdS nanomaterials also relatively decreased the photocurrent of the modified electrode (curve '*d*'), which was ascribed to the fact that the photogenerated charge carrier recombination in the PEC sensing system was significantly inhibited by special Z-scheme electron shuttle. The reason for higher photocurrent of CdS-WO_3/FTO than that of Au-WO_3/FTO was attributed to the fact that CdS and WO_3 could be used as the donor and acceptor of the electrons for the generation of photocurrent. Therefore, Z-scheme CdS-Au-WO_3 could enhance the photocurrent of the photosensitive electrode in the simultaneous presence of CdS, Au and WO_3 nanostructures.

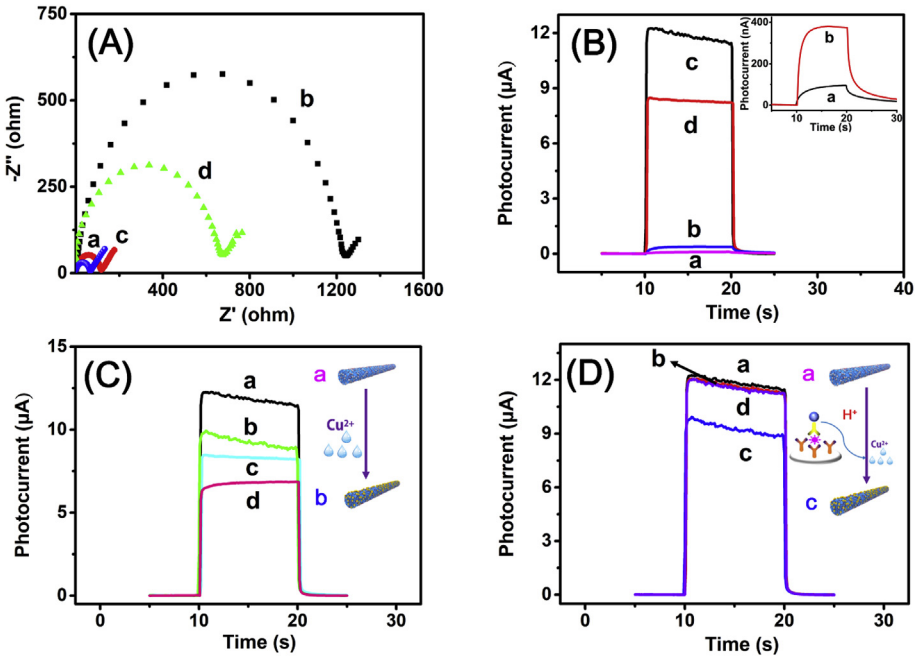

Fig. 2. (A) Nyquist plots of (a) FTO electrode, (b) WO_3/FTO, (c) Au-WO_3/FTO and (d) CdS-Au-WO_3/FTO in PBS (0.1 M, pH 7.4) containing $Fe(CN)_6^{4-/3-}$ (5.0 mM) within the range from 10^{-2}–10^5 Hz at an alternate voltage of 5 mV; (B) Photocurrents of (a) WO_3/FTO, (b) Au-WO_3/FTO, (c) CdS-Au-WO_3/FTO and (d) CdS-WO_3/FTO; (C) Photocurrents of (a,d) CdS-Au-WO_3/FTO and (b,c) WO_3-CdS in the absence (a,b) and presence (c,d) Cu^{2+} ion; (D) Photocurrents of CdS-Au-WO_3-based PEC immunoassay in the absence (b) and presence (c) of target PSA (1.0 ng mL^{-1} used in this case) relative to background signal of (a) CdS-Au-WO_3/FTO (note: Curve '*d*' represents the photocurrent of CdS-Au-WO_3/FTO after reaction with the mixture containing mAb, PSA and pAb). All the PEC measurements were carried out in PBS (0.1 M, pH 7.0).

3.3. Evaluation of feasibility and control experiments

As described above, the photocurrent of CdS-Au-WO_3-modified FTO electrode could be decreased in the presence of Cu^{2+}. To verify this point, the photocurrents of CdS-Au-WO_3/FTO were monitored upon addition of Cu^{2+} ion in the detection solution. As seen from curve '*d*' in Fig. 2C, the photocurrent of CdS-Au-WO_3/FTO with Cu^{2+} ion decreased relative to curve '*a*' without it, indicating that Cu^{2+} ion could quench the photocurrent. To highlight the advantage of gold nanoparticles in the Z-scheme system, we also evaluated the change of CdS-WO_3-modified FTO electrode in the photocurrent toward Cu^{2+} ion as the control experiment. Similarly, the photocurrent decreased upon Cu^{2+} ion introduction. Significantly, the change of photocurrent at the CdS-Au-WO_3/FTO was clearly more than that of CdS-WO_3/FTO, suggesting the enhanced efficiency of gold nanoparticles in the Z-scheme system. In addition, these results further indicated that Cu^{2+} ion could be used as the quencher for the CdS-Au-WO_3 photoactive materials.

Typically, Cu^{2+} ions can be released by using CuO nanoparticles under acidic conditions. By using CuO nanoparticle-labeled antibody, a CdS-Au-WO_3-based PEC immunoassay was developed for the detection of target PSA with a sandwich-type assay format, as described in the Experimental section. As indicated in Fig. 2D, the photocurrent of PEC immunoassay in the absence of target PSA (curve '*b*') was almost the same as the background signal of CdS-Au-WO_3/FTO (curve '*a*'), while the photocurrent sharply decreased in the presence of target PSA (curve '*c*'). As control test, 20 μL of 1.0 mM HCl solution containing mAb, PSA and pAb was directly determined on the CdS-Au-WO_3/FTO, and the obtained photocurrent (curve '*d*') slightly decreased in comparison with background signal (curve '*a*'), indicating that the decreasing photocurrent of CdS-Au-WO_3/FTO derived from the labeled CuO nanoparticles on the detection antibody under acidic conditions. Through the interaction of CdS in the Z-scheme system with the released Cu^{2+} ion, the produced Cu_xS impeded the electron transfer thanks to the generation of the new energy levels for electron-hole recombination (Scheme 1). Hence, PEC immunoassay could be employed to detect target PSA on the CdS-Au-WO_3/FTO by using CuO-labeled secondary antibody.

3.4. Optimization of experimental conditions

To achieve a high sensitivity of CdS-Au-WO_3-modified FTO electrode, the following parameters were optimized such as the number of CdS coating on the Au-WO_3-modified FTO electrode, the pH of 0.1 M PBS detection solution and the immunoreaction time for the formation of immunocomplex. In this photosensitive system, the light was captured by CdS nanoparticles. The capture efficiency relied on the thickness of CdS nanoparticles. As shown in Fig. 3A, the maximum photocurrent was obtained at the number of 4 coating CdS. Typically, a low-amount CdS was unfavorable for the light adsorption, whereas a high-amount CdS increased diffusion resistance of electron transfer and formed many recombination centers (Han et al., 2018; Wang et al., 2017c). So, 4 of the coating CdS layers were used for the fabrication of Z-scheme CdS-Au-WO_3 nanocomposites.

Similarly, the photocurrents of CdS-Au-WO_3-modified FTO electrode relied on the pH of detection solution. As exhibited in Fig. 3B, the photocurrents initially increased with the increasing pH of PBS, and then decreased. An optimum photocurrent was achieved in pH 7.0 PBS. At the pH values of below 7.0, H^+ ion acted as the competitor of Cu^{2+} ion to consume photogenerated electrons of CdS for formation of H_2 (Wang et al., 2010). A high-pH solution was favorable for Cd^{2+} exposed on the surface defect sites of CdS nanoparticles to adsorb the OH^- and inhibit the contact of the electrons of nanoparticles with electron acceptor (O_2), thereby resulting in the decreeing photocurrent (Lin et al., 2016; Zang et al., 2014). Hence, pH 7.0 of 0.1 M PBS was used as the supporting electrolyte for PEC measurement.

In addition, the immunoreaction time directly affects the sensitivity of PEC immunoassay. Usually, the antigen-antibody reaction rate increases with the increasing time, then gradually decreases, and then tends to the dynamic equilibrium. To avoid confusion, the reaction time of mAb with target PSA was paralleled with those of PSA-mAb with CuO NP-pAb in this case. As seen from Fig. 3C, the photocurrent reached a plateau after 40 min. A longer immunoreaction time did not cause significant increase of the photocurrent. To save the assay time, 40 min of immunoreaction time was selected for the formation of immunocomplex.

3.5. Analytical performance of CdS-Au-WO_3-based PEC immunoassay

By using Z-scheme CdS-Au-WO_3 as the photoactive materials, PSA standards with different levels were determined by the developed PEC immunosensing platform under optimum conditions. The labeled CuO NP on the detection antibody was used as the quencher of photoactive materials under acidic solution. As indicated in Fig. 4A, the photocurrents decreased with the increment of target PSA concentrations. A good linear relationship between the photocurrent and the decimal logarithm of PSA level was acquired within the dynamic range of 0.01–50 ng mL^{-1}. The linear regression equation was as follows: I (μA) = 8.884–1.057 × log($C_{[PSA]}$/ng mL^{-1}) (R^2 = 0.9979, n = 8). The limit of detection (LOD) was evaluated to 1.8 pg mL^{-1} at 3σ (where σ is the standard deviation of a blank sample, n = 11). To further embody the merits of Z-scheme CdS-Au-WO_3-based PEC immunoassay, the analytical properties of our system including the linear range and LOD were compared with other PSA detection schemes. As analyzed from Table S1 in the Supporting Information, the LOD of our strategy was comparable with those of other methods, despite a relatively narrow linear range in comparison with partial detection platforms. The reason was attributed to the fact that the released Cu^{2+} ions from the nanoparticles in the microplate were diluted to 5.0 mL PBS (0.1 M, pH 7.0) detection solution during the photocurrent measurement. Since the threshold of PSA in normal human serum is 4.0 ng mL^{-1} (Yang et al., 2010), our strategy completely meets the needs of PSA detection in clinic diagnosis.

Next, the stability and life time of the as-prepared CdS-Au-WO_3/FTO electrode were studied as follows. First, we monitored the stability of the modified electrode during continuous photocurrent measurements under the 'on-off' light irradiation. As shown in Fig. 4C, all the

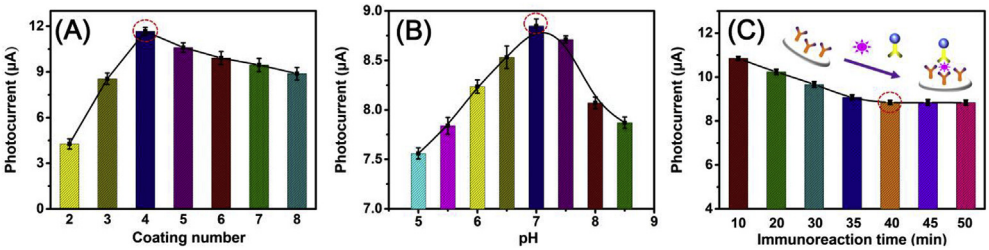

Fig. 3. Effects of (A) coating number of CdS, (B) pH of PBS detection solution, and (C) immunoreaction time on the photocurrent of CdS-Au-WO_3-modified FTO electrode (1.0 ng mL^{-1} PSA used in these cases).

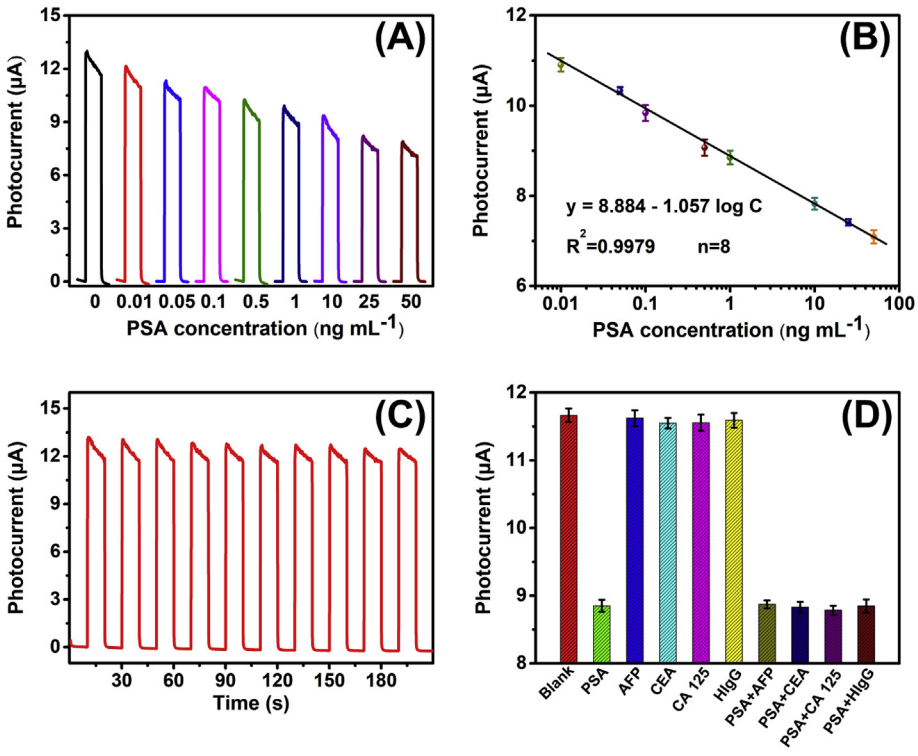

Fig. 4. (A) Photocurrent responses of Z-scheme CdS-Au-WO_3-based PEC immunoassay toward PSA standards in pH 7.0 PBS (0.1 M); (B) calibration plots; (C) the stability of CdS-Au-WO_3-modified FTO electrode under the continuous measurements; (D) the specificity of Z-scheme CdS-Au-WO_3-based PEC immunoassay against target PSA and non-targets including AFP, CEA, CA 125 and HIgG (note: 1.0 ng mL^{-1} for target PSA and 100 ng mL^{-1} for non-target analytes).

Table 1
Accuracy evaluation of Z-scheme CdS-Au-WO_3-based PEC immunoassay method relative to human PSA ELISA kit for human serum specimens.

Sample no.	Method; Conc. (mean ± SD, ng mL^{-1}, n = 3)		t_{exp}
	PEC immunoassay	ELISA kit	
1	23.58 ± 2.46	21.43 ± 2.08	1.16
2	7.38 ± 0.53	8.03 ± 0.41	1.68
3	3.69 ± 0.19	3.41 ± 0.20	1.76
4	18.54 ± 1.89	21.04 ± 1.59	1.75
5	12.59 ± 1.25	11.03 ± 1.09	1.63
6	1.43 ± 0.09	1.51 ± 0.10	1.03
7	16.13 ± 1.39	18.39 ± 1.13	2.19
8	28.75 ± 2.49	26.31 ± 2.45	1.21

photocurrents were almost the same at the 'on' and 'off' states, respectively. The relative standard deviations (RSDs) for the photocurrents were 5.3% and 3.1% (n = 10) for the 'on' and 'off' states, respectively. Subsequently, the storage stability of the prepared CdS-Au-WO_3/FTO and CuO NP-pAb was determined during a six-month storage period. They were stored at 4 °C when not in use. By using 1.0 ng mL^{-1} PSA as an example, the photocurrents could preserve 98.8%, 96.2%, 95.7%, 93.6%, 90.8% and 87.4% of the initial signal after storage them at 1st, 2nd, 3rd, 4th, 5th and 6th months, respectively, suggesting a long-time stability. Furthermore, the reproducibility of PEC immunoassay was evaluated by analyzing 1.0 ng mL^{-1} PSA with six parallel measurements, and the RSD was ~8.46% (n = 6) with good precision.

Except for selectivity and reproducibility, the specificity of PEC immunoassay were monitored by analyzing other possible biomarkers, *e.g.*, alpha-fetoprotein (AFP), carcinoembryonic antigen (CEA), cancer antigen 125 (CA 125) and human IgG (HIgG). Fig. 4D displays the experimental results. Obviously, the strong shifts in the photocurrent relative to background signal could be only observed in the presence of target PSA. Importantly, the coexistence of non-targets with PSA did not cause the significant change of the photocurrent in comparison with target PSA alone. Thus, Z-scheme CdS-Au-WO_3-based PEC immunoassay had good selectivity for target PSA.

3.6. Screening of human serum specimens

To investigate the accuracy of the newly developed method, Z-scheme CdS-Au-WO_3-based PEC immunoassay was used for analysis of human serum specimens. Initially, we collected eight human serum samples including target PSA from Fujian Provincial Hospital, China, according to the rules of the local ethical committee. Informed consent was obtained from any experimentation with human subjects. Following that, these samples were determined by using our developed PEC immunoassay (note: All handing and processing were performed carefully during the measurements, and all the tools in contact with patient specimens were disinfected after use), and the obtained results were compared with those from human ELISA kit. All data are presented in Table 1. The accuracy of this method was evaluated on the basis of a classical t-test relative to commercial human ELISA kit. Obviously, no significant difference at the 0.05 significance level were encountered in the analysis of 8 clinical serum samples between the developed PEC immunoassay and the commercially available ELISA kits for detection of target PSA because all the t_{exp} values in all cases were below t_{crit} ($t_{crit[4,\ 0.05]}$ = 2.77). Hence, Z-scheme CdS-Au-WO_3-based PEC immunoassay could be preliminarily applied for the determination of PSA in biological fluids.

4. Conclusions

In summary, this work successfully demonstrated an all-solid-state CdS-Au-WO_3-based Z-scheme photoelectrochemical immunoassay for quantitative monitoring of disease-related biomarker (PSA used as an example). CuO nanoparticles were used as the labels of the detection antibody to release the quencher of CdS-Au-WO_3 photoactive materials. Compared to conventional PEC immunoassays, highlights of this study can be summarized as follows: (i) the immunoreaction and PEC measurement are carried out in different reaction and detection cells, thus effectively avoiding the interfering of biomolecules; (ii) introduction of gold nanoparticles between CdS and WO_3 can enhance the signal of PEC

detection system as a result of effective charge separation between WO_3 and CdS driven by gold nanoparticles (solid electron mediators); (iii) CuO NP-based immunoassay does not need the participation of nature enzyme; and (iv) CuO NP-based nano label can release number Cu^{2+} ions under acidic conditions to quench the photocurrent of CdS-Au-WO_3 materials. Nevertheless, one disadvantage of this system is a relatively long time for the formation of sandwiched immunocomplex. Actually, this shortcoming can be overcome by using two monoclonal antibodies with different clone numbers. Future work should be focused on improvement of the immune reaction mode.

Acknowledgments

Authors acknowledged financial support from the National Natural Science Foundation of China (Grant nos.: 21675029 & 201874022) and the Health-Education Joint Research Project of Fujian Province (Grant no.: WKJ2016-2-15).

Appendix A. Supplementary data

Supplementary data to this article can be found online at https://doi.org/10.1016/j.bios.2019.03.052.

References

Barber, J., 2009. Chem. Soc. Rev. 38, 185–196.
Fan, G., Ren, X., Zhu, C., Zhang, J., Zhu, J., 2014. Biosens. Bioelectron. 59, 45–53.
Favereau, L., Makhal, A., Pellegrin, Y., Blart, E., Petersson, J., Göransson, E., Hammarström, L., Odobel, F., 2016. J. Am. Chem. Soc. 138, 3752–3760.
Gao, C., Xue, J., Zhang, L., Cui, K., Li, H., Yu, J., 2018. Anal. Chem. 90, 14116–14120.
Han, Q., Wang, R., Xing, B., Zhang, T., Khan, M., Wu, D., Wei, Q., 2018. Biosens. Bioelectron. 99, 493–499.
Iwase, A., Ng, Y., Ishiguro, Y., Kudo, A., Amal, R., 2011. J. Am. Chem. Soc. 133, 11054–11057.
Iwase, A., Yoshino, S., Takayama, T., Ng, Y., Amal, R., Kudo, A., 2016. J. Am. Chem. Soc. 138, 10260–10264.
Jiang, J., He, Y., Wan, L., Cui, Z., Cui, Z., Jessop, P., 2013. Chem. Commun. 49, 1912–1914.
Jiang, K., Weng, Y., Guo, S., Yu, Y., Xiao, F., 2017. Nanoscale 9, 16922–16936.
Kong, Q., Cui, K., Zhang, L., Wang, Y., Sun, J., Ge, S., Zhang, Y., Yu, J., 2018. Anal. Chem. 90, 11297–11304.
Kothe, T., Plumere, N., Badura, A., Nowaczyk, M., Guschin, D., Rogner, M., Schuhmann, W., 2013. Angew. Chem. Int. Ed. 52, 14233–14236.
Li, H., Yu, H., Quan, X., Chen, S., Zhang, Y., 2016. ACS Appl. Mater. Interfaces 8, 2111–2119.
Li, P., Zhou, Y., Li, H., Xu, Q., Meng, X., Wang, X., Xiao, M., Zou, Z., 2015. Chem. Commun. 51, 800–803.
Liang, M., Borjigin, T., Zhang, Y., Liu, H., Liu, B., Guo, H., 2018. ACS Appl. Mater. Interfaces 10, 34123–34131.
Lin, Y., Zhou, Q., Tang, D., Niessner, R., Yang, H., Knopp, D., 2016. Anal. Chem. 88, 7858–7866.
Liu, Y., Li, R., Gao, P., Zhang, Y., Ma, H., Yang, J., Du, B., Wei, Q., 2015. Biosens. Bioelectron. 65, 97–102.
Luo, Z., Zhang, L., Zeng, R., Su, L., Tang, D., 2018. Anal. Chem. 90, 9568–9575.
Lv, S., Zhang, K., Zeng, Y., Tang, D., 2018. Anal. Chem. 90, 7086–7093.
Park, S., Lee, I., Park, J., 2013. Org. Biomol. Chem. 11, 395–399.
Pu, Y., Wang, G., Chang, K., Ling, Y., Lin, Y., Fitzmorris, B., Liu, C., Lu, X., Tong, Y., Zhang, J., Hsu, Y., Li, Y., 2013. Nano Lett. 13, 3817–3823.
Qiu, Z., Shu, J., Tang, D., 2018. Anal. Chem. 90, 1021–1028.
Qu, W., Liu, Y., Liu, D., Wang, Z., Jiang, X., 2011. Angew. Chem. Int. Ed. 50, 3442–3445.
Sun, B., Chen, L., Xu, Y., Liu, M., Yin, H., Ai, S., 2014. Biosens. Bioelectron. 51, 164–169.
Tachibana, Y., Vayssieres, L., Durrant, J., 2012. Nat. Photon. 6, 511.
Tada, H., Mitsui, T., Kiyonaga, T., Akita, T., Tanaka, K., 2006. Nat. Mater. 5, 782.
Tang, J., Li, J., Zhang, Y., Kong, B., Wang, Y., Quan, Y., Cheng, H., Al-Enizi, A., Gong, X., Zheng, G., 2015. Anal. Chem. 87, 6703–6708.
Tu, W., Cao, H., Zhang, L., Bao, J., Liu, X., Dai, Z., 2016. Anal. Chem. 88, 10459–10465.
Wang, G., Xu, J., Chen, H., 2010. Nanoscale 2, 1112–1114.
Wang, Q., Hisatomi, T., Jia, Q., Tokudome, H., Zhong, M., Wang, C., Pan, Z., Takata, T., Nakabayashi, M., Shibata, N., Li, Y., Sharp, I., Kudo, A., Yamada, T., Domen, K., 2016. Nat. Mater. 15, 611.
Wang, Y., Ge, S., Zhang, L., Yu, J., Yan, M., Huang, J., 2017a. Biosens. Bioelectron. 89, 859–865.
Wang, Q., Hisatomi, T., Suzuki, Y., Pan, Z., Seo, J., Katayama, M., Minegishi, T., Nishiyama, H., Takata, T., Seki, K., Kudo, A., Yamada, T., Domen, K., 2017b. J. Am. Chem. Soc. 139, 1675–1683.
Wang, R., Ma, H., Zhang, Y., Wang, Q., Yang, Z., Du, B., Wu, D., Wei, Q., 2017c. Biosens. Bioelectron. 96, 345–350.
Wang, Y., Suzuki, H., Xie, J., Tomita, O., Martin, D., Higashi, M., Kong, D., Abe, R., Tang, J., 2018. Chem. Rev. 118, 5201–5241.
Weng, B., Wu, J., Zhang, N., Xu, Y., 2014. Langmuir 30, 5574–5584.
Yang, M., Javadi, A., Li, H., Gong, S., 2010. Biosens. Bioelectron. 26, 560–565.
Yang, T., Li, C., He, J., Chen, B., Li, Y., Huang, C., 2018. Anal. Chem. 90, 9966–9974.
Yun, H., Lee, H., Kim, N., Lee, D., Yu, S., Yi, J., 2011. ACS Nano 5, 4084–4090.
Zang, Y., Lei, J., Zhang, L., Ju, H., 2014. Anal. Chem. 86, 12362–12368.
Zhao, W., Xu, J., Chen, H., 2014. Chem. Rev. 114, 7421–7441.
Zhao, W., Xu, J., Chen, H., 2015. Chem. Soc. Rev. 44, 729–741.
Zhao, W., Xu, J., Chen, H., 2017. Biosens. Bioelectron. 92, 294–304.
Zhou, P., Yu, J., Jaroniec, M., 2014. Adv. Mater. 26, 4920–4935.